

Frequency domain triangulation for full-field 3D operating-deflection-shape identification

Domen Gorjup^a, Janko Slavič^{a,*}, Miha Boltežar^a

^aUniversity of Ljubljana, Faculty of Mechanical Engineering, Aškerčeva 6, 1000 Ljubljana, Slovenia

Cite as:

Domen Gorjup, Janko Slavič, Miha Boltežar, Frequency domain triangulation for full-field 3D operating-deflection-shape identification, Mechanical Systems and Signal Processing, Volume 133, 2019, 106287, ISSN 0888-3270, <https://doi.org/10.1016/j.ymsp.2019.106287>.

Abstract

The use of high-speed camera systems in vibration measurements is typically limited to identifying motion, transversal to the optical axis, due to an inherent limitation of 2D imaging systems. Depth information, lost in the imaging process, can be recovered by using the well-established 3D DIC technique, but is still limited to a single face of the object, observed by the stereo pair. In this research a full-field 3D operating-deflection-shape measurement technique, based on frequency-domain triangulation of image-data, is presented. A mathematical model of frequency-domain perspective transformation of small harmonic motion is introduced. This model is used to relate multiview image data to spatial amplitude spectra of the observed displacement. Using the developed method, spatial small harmonic motion of arbitrary-shaped specimen can be identified in the frequency domain using only a single, moving high-speed camera, extending the field-of-view of the established image-based vibration measurement methods.

Keywords: digital image correlation, full-field displacement measurement, single-camera, spatial operating-deflection-shapes, multiview geometry, frequency domain, triangulation

1. Introduction

Due to their high spatial resolution and non-contacting nature, image-based methods have become a well-established alternative to conventional vibration

*Corresponding author

Email address: janko.slavic@fs.uni-lj.si (Janko Slavič)

measurement techniques. In cases where a large number of measured degrees-of-freedom is required, the use of piezoelectric accelerometers is highly impractical, and the effects of added mass make them unusable in applications where the measured object is very lightweight or small in size.

For the reasons outlined above, various optical methods for vibration measurements have been developed. Scanning Laser Doppler Vibrometry (SLDV) is one of the most established. It utilizes the Doppler effect to measure the velocity of a point on the observed surface in the direction of a laser beam. Using multiple laser heads and a scanning technique, spatial measurements for multiple degrees of freedom can be obtained, as described by Reu et al. [1]. A relatively slow data-acquisition process and the complexity of system calibration are known limitations of SLDV. Interferometric methods, such as Holographic Interferometry [2] and Electronic Speckle Pattern Interferometry (ESPI) [3], are also used in vibration measurements. They offer a non-contacting way of identifying full-field displacements by observing the interference patterns of laser light, reflected from the surface of a vibrating structure, and can be used to measure spatial vibrations [4].

With developments in high-speed camera technology, displacement measurement techniques based on digital image processing have steadily been gaining popularity in the field of vibration testing, with works by authors such as Helfrick et al. [5] and Wang et al. [6]. Photogrammetric point-tracking [7, 8], gradient-based displacement identification [9], digital image correlation (DIC) [10] and motion magnification [11, 12] are among the most frequently used, with novel methods still regularly being introduced, e.g. spectral optical flow imaging (SOFI) [13]. A lot of recent work has been focused on gradient-based and image-correlation methods in particular [14]. State-of-the-art techniques allow for identification of modal parameters with displacement amplitudes as low as 10^{-5} pixel, as demonstrated by Javh et al. [15, 16], and efforts are still being made to improve their performance, e.g. through efficient data compression [17], intelligent handling of non-ideal operating conditions [18] or realistic visualization of the full-field dynamic response [19]. Furthermore, 3D DIC is already considered a valid alternative to the more traditional methods of measuring 3D structural vibrations by authors such as Helfrick et al. [5] or Bebernis and Ehrhardt [20]. In 3D digital image correlation, depth information, lost in the imaging process, can be recovered by utilizing multiview triangulation with a pair of time-synchronized high-speed cameras [21]. Its field of view is, however, usually limited to a single face of the vibrating structure, observed by the stereo pair, as stated by Patil et al. [22].

When observing complex-shaped 3D objects, multiview geometry principles can be used to extend the imaging system's field of view [23]. Numerous approaches to multiview 3D displacement measurements have been introduced, varying in camera configuration and the principle of operation, as is evident from Pan's recent review of the field [14]. Multiview systems analyse corresponding points in images, synchronously acquired by cameras with different positions and orientations relative to the subject, to acquire spatial measurements through triangulation [24, 25], or compose a complete measurement from individually

acquired sets of stereo-DIC results. The surface-stitching method of combining deflection shapes measured by a moving stereo pair of time-synchronized cameras is another multiview technique used in vibration measurement [26, 27]. System calibration and correspondence matching add a layer of complexity compared to conventional 3D DIC.

Distortions in the optical systems, as well as inaccuracies in the synchronization of cameras used for simultaneous multiview image acquisition, can have an adverse effect on the measurement results [28]. Lower complexity, compactness and cost-effectiveness have made the prospect of so-called single-camera multiview systems a prominent research subject in recent years. Most such systems utilize light-splitting elements, namely mirror adapters [29, 30], prisms [31] or other optical devices [32], to project multiple views of the observed object onto a single image sensor. A method using a beam-splitter prism combined with a color high-speed camera has recently been introduced by Yu and Pan [33]. Single-camera multiview digital image correlation using mirror adapters has also been applied to vibration measurements by Yu and Pan [34], as well as Durand-Texte et al. [35]. The use of specialized equipment and, in some cases, reduced spatial resolution are often cited as limitations of existing single-camera multiview systems.

In this work, a novel single-camera multiview operating-deflection-shape measurement method is introduced. The properties of the stationary vibrating response of linear, time-invariant mechanical structures are leveraged by performing the multiview triangulation of image-based displacement measurements in the frequency domain, producing full-field 3D operating-deflection-shape measurements using only a single monochrome high-speed camera.

This paper is organised as follows. Section 2 gives an overview of image-based displacement measurements, multiview imaging and operating-deflection-shape measurements. In Section 3 a mathematical model of the perspective-camera projection of small harmonic motion in the frequency domain is introduced. Section 4 extends Section 3 by introducing the single-camera multiview operating-deflection-shape identification method with triangulation in the frequency domain. Section 5 presents the experimental work and Section 6, the conclusions.

2. Theoretical background

The image-processing stage of the proposed single-camera multiview operating-deflection-shape identification method can be broken down into two steps:

1. 2D displacement identification in each distinct moving camera view for a single measurement.
2. Multiview imaging system calibration and the triangulation of spatial displacement information.

This section outlines the basics of both of the above-mentioned stages of the measurement process, and points the reader to further information on the subject.

As the resulting spatial displacement data is used as the input for operating-deflection-shape identification in this work, a brief overview of this field is also provided.

2.1. Image-based displacement identification

One of the computationally most efficient methods of extracting 2D displacement information based on a sequence of grayscale images is the Gradient-based optical flow estimation [36] method. It is based on the optical flow constraint:

$$I(u, v, t) = I(u + \Delta u, v + \Delta v, t + \Delta t) \quad (1)$$

where $I(u, v, t)$ denotes the brightness of an image element at position (u, v) at a specific time t , and Δu and Δv are the image translation parameters to be identified. From the first-order Taylor expansion of (1), the following linear relation between consecutive image-brightness values and the displacement can be derived for a single image pixel, acting now as a displacement sensory element [15]:

$$s(u, v) = \frac{f(u, v) - g(u, v)}{|\nabla f(u, v)|} \quad (2)$$

where $f(u, v)$ and $g(u, v)$ denote the reference image $I(u, v, t)$ and the displaced image $I(u, v, t + \Delta t)$, respectively. Due to the aperture problem, only the displacement s in the direction of the local reference image-brightness gradient $\nabla f(u, v)$ can be calculated using the gray-value data of a single pixel [15]. Observing a $(2M + 1) \times (2M + 1)$ subset of pixels, performing a first-order Taylor expansion of (1) yields an overdetermined system of linear equations, for which the closed-form least-squares solution is [36]:

$$\begin{bmatrix} \Delta u \\ \Delta v \end{bmatrix} = - \begin{bmatrix} \sum g_u^2 & \sum g_u g_v \\ \sum g_u g_v & \sum g_v^2 \end{bmatrix}^{-1} \begin{bmatrix} \sum g_u (g - f) \\ \sum g_v (g - f) \end{bmatrix} \quad (3)$$

where g_u and g_v are the numerically calculated first-order derivatives of the displaced image in the u and v directions, respectively, and the summations are performed over all the pixels in the subset.

Perhaps the most frequently used method of image-based displacement identification is Digital Image Correlation (DIC). It employs an iterative optimization procedure to minimize the difference between a region of interest in the reference image $f(u, v)$ and each consecutive image in the video sequence $g(\xi(u, v, \mathbf{r}))$, to which a geometric coordinate transformation $\xi(u, v, \mathbf{r})$ with parameters \mathbf{r} was applied, as shown in Fig. 1.

This can be achieved by minimizing the sum of the squared difference cost function:

$$SSD = \sum \left(f(u, v) - g(\xi(u, v, \mathbf{r})) \right)^2 \quad (4)$$

but different cost functions might be preferable in some cases [14, 37]. By determining the optimal values of the geometric transformation parameters \mathbf{r} ,

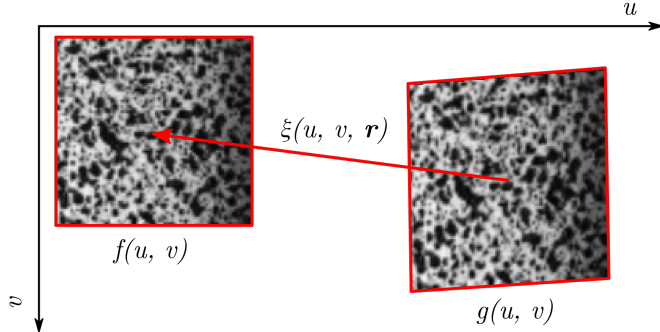


Figure 1: DIC principle of operation.

displacements and deformations of the observed region of interest are recovered. Different shape functions $\xi(u, v, \mathbf{r})$ are chosen to adjust the performance and the computational efficiency of the method [38].

For the simple translation case:

$$\xi(u, v, \mathbf{r}) = \begin{cases} u + r_0 \\ v + r_1 \end{cases} \quad (5)$$

a single iteration of the DIC method using the SSD cost function (4) is equivalent to the least-squares solution to the gradient-based optical flow system of equations for a subset of pixels (3) [38].

It is worth noting that, although the spatial information in a digital image is discretized to integer pixel locations, the transformed coordinates $\xi(u, v, \mathbf{r})$ generally do not fall onto this discrete grid. To evaluate $g(\xi(u, v, \mathbf{r}))$ for non-integer locations, image interpolation is performed. Coincidentally, the identified displacement parameters are not limited to integer values. This is also true for displacements, identified using the gradient-based method in Eq. (2) or Eq. (3), and indeed, the displacement amplitudes, accurately identified in such measurements, can be as low as 10^{-3} pixel using state-of-the-art methods [15].

2.2. Multiview imaging and the linear triangulation method

In a multiview imaging system, each view is defined by a perspective mapping between the 3D coordinates of a point $\mathbf{U} = \{U, V, W\}^T$ in Euclidean space and its projection $\mathbf{u} = \{u, v\}^T$ in a 2D image. To facilitate this projective transformation, the points \mathbf{U} and \mathbf{u} are represented in homogeneous coordinates [23]:

$$\begin{aligned} \mathbf{U} &= \{U, V, W, 1\}^T \\ \mathbf{u} &= \{u, v, 1\}^T \end{aligned} \quad (6)$$

and the image-projection of \mathbf{U} in homogeneous coordinates is:

$$w \mathbf{u} = \mathbf{P} \mathbf{U} \quad (7)$$

where \mathbf{P} is a linear projective mapping from \mathbb{P}^3 to \mathbb{P}^2 , often termed the camera matrix. The image-coordinates \mathbf{u} of the imaged point \mathbf{U} in Euclidean space are obtained by dividing the result of Eq. (7) by the scale factor w :

$$w = \mathbf{p}^3 \mathbf{U} \quad (8)$$

where \mathbf{p}^3 denotes the third row of \mathbf{P} , and dropping the last coordinate, added in (6). As the scale factor w is dependent on \mathbf{U} (8), the perspective transformation is non-linear in the Euclidean coordinate frame [23].

Homogeneous representation of points is in this research only used where the projective transformation (7) is being performed. In all other cases, and once the projective transformation result has been normalized by the perspective scale factor (8), all points are represented in Euclidean coordinates.

The camera matrix \mathbf{P} (7) can be further decomposed as $\mathbf{P} = \mathbf{K} [\mathbf{R}|\mathbf{t}]$ into a calibration matrix \mathbf{K} containing the camera's intrinsic parameters, such as the focal length and the optical centre, and a 3×4 matrix of extrinsic parameters $[\mathbf{R}|\mathbf{t}]$, composed of a rotation matrix \mathbf{R} and a translation vector \mathbf{t} , which together describe the camera's position in a chosen reference coordinate frame. For the pinhole camera model, Eq. (7) can be written as [23]:

$$\begin{aligned} w \mathbf{u} &= \mathbf{K} [\mathbf{R}|\mathbf{t}] \mathbf{U} \\ &\Downarrow \\ \begin{Bmatrix} w u \\ w v \\ w \end{Bmatrix} &= \begin{bmatrix} k_{1,1} & k_{1,2} & k_{1,3} \\ 0 & k_{2,2} & k_{2,3} \\ 0 & 0 & k_{3,3} \end{bmatrix} \begin{bmatrix} r_{1,1} & r_{1,2} & r_{1,3} & t_1 \\ r_{2,1} & r_{2,2} & r_{2,3} & t_2 \\ r_{3,1} & r_{3,2} & r_{3,3} & t_3 \end{bmatrix} \begin{Bmatrix} U \\ V \\ W \\ 1 \end{Bmatrix} \end{aligned} \quad (9)$$

The process of determining the intrinsic and extrinsic parameters and thus the matrices \mathbf{P} for each camera view (see Fig. 2) is termed the calibration of a multiview imaging system [23]. This can be achieved using images of a planar calibration pattern, positioned in each camera view [39, 40]. Alternatively, if the same optical system is used throughout the multiview measurement, its intrinsic calibration matrix \mathbf{K} can be determined in advance. If the geometry of the observed object is known, this information can then be used to precisely determine the extrinsic parameters of every measurement view and define the global coordinate frame of the measurement, by solving the Perspective-n-Point problem [41] for reference images in each distinct view.

The perspective transformation, described in Eq. (7) maps multiple points on the camera's optical axis to a single image point \mathbf{u} (Fig. 2) and is non-invertible (the spatial coordinates of \mathbf{U} can not be calculated directly from a single image \mathbf{u}). However, with a calibrated camera, where the matrix \mathbf{P} is known, the third equation of (9) can be used to eliminate the unknown scale factor w (8) from the first two equations of (9) [42]:

$$\begin{aligned} w u &= (\mathbf{p}^3 \mathbf{U}) u = \mathbf{p}^1 \mathbf{U} \\ w v &= (\mathbf{p}^3 \mathbf{U}) v = \mathbf{p}^2 \mathbf{U} \end{aligned} \quad (10)$$

where \mathbf{p}^i denotes the i -th row of \mathbf{P} . In a single calibrated camera view, Eq. (10) gives us two equations, linear in the three unknown coordinates of \mathbf{U} . Determining the location of the point \mathbf{U} in another calibrated view gives us two additional equations (10). With at least two different views of the same physical point, we therefore have enough equations to triangulate its position \mathbf{U} in space.

In general, for an n -view imaging setup we obtain a system of $2n$ equations (10), linear in the three unknowns of \mathbf{U} . Solving this system of linear equations is equivalent to finding the intersection of rays, projected through the image points from each camera centre [23], which is illustrated for four views in Fig. 2. The projected rays do not necessarily intersect due to errors in the imaging process and system calibration, and the solution to this overdetermined system is approximated in a least-squares sense to determine the 3D point \mathbf{U} from image measurements [42].

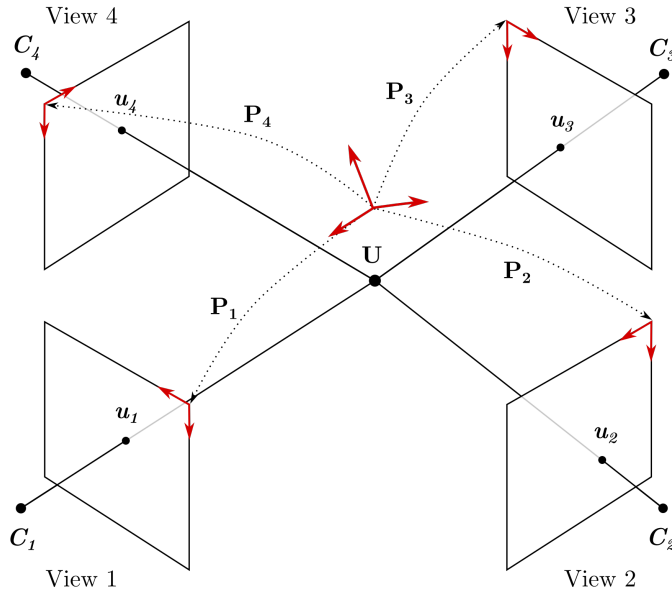


Figure 2: Multiview triangulation example. C_j represents the optical centre of camera j .

2.3. Operating-deflection-shape measurement

A spatial model describing the forced response $\mathbf{x}(t)$ of a multiple-degree-of-freedom (MDOF) mechanical system is characterized by the following equilibrium equation:

$$\mathbf{M} \ddot{\mathbf{x}}(t) + \mathbf{C} \dot{\mathbf{x}}(t) + \mathbf{K} \mathbf{x}(t) = \mathbf{f}(t) \quad (11)$$

where $\mathbf{f}(t)$ is the vector of applied excitation forces for each degree of freedom, and \mathbf{M} , \mathbf{C} and \mathbf{K} are the mass, damping and stiffness matrices, respectively [43]. The relation between the response amplitudes \mathbf{x} and the amplitudes of

the excitation force \mathbf{f} in the frequency domain, derived from (11) for harmonic excitation, constitutes the response model of the structure:

$$\mathbf{X}(\omega) = \mathbf{H}(\omega) \mathbf{F}(\omega) \quad (12)$$

where $\mathbf{H}(\omega)$ is a complex receptance frequency response function (FRF) matrix. The FRFs can be further expressed in terms of the structure's natural frequencies, mode shapes and damping factors to facilitate the identification of the modal parameters in the experimental modal analysis [43].

The measured response values of a vibrating structure for multiple degrees of freedom at a specific point in time, $\mathbf{x}(t)$, or at a specific frequency, $\mathbf{X}(\omega)$, constitute the structure's operating-deflection-shape (ODS) [44]. In expressing the ODS of a structure in terms of its FRFs (12) and, consequently, its mode shapes, we assume the linearity of the structure's response [44].

For stationary excitation the observed ODS is also stationary [45], and response measurements need not be performed simultaneously to produce valid deflection-shape magnitudes. The errors in phase of the measured response due to nonsynchronous data acquisition can be corrected in post-processing, using a reference response measurement [45].

3. Perspective camera projection of small harmonic motion in the frequency domain

To reconstruct spatial harmonic motion spectra by triangulating image information, frequency-domain images of the motion must be constructed for each camera view. In this section, the perspective-camera projection of harmonic, relatively (compared to the dimensions of the observed scene) small-amplitude motion is examined.

A particular point in space, oscillating at frequency ω_k with complex-valued spatial amplitude $\Delta \mathbf{U}(\omega_k)$ around an initial position \mathbf{U}^{REF} , is observed by a perspective camera (9). At the time the n -th image is sampled, $\mathbf{U}(t_n)$ is the 3D position of the observed point and the image-measured displacement $\Delta \mathbf{u}(t_n)$ is the difference between the current and the reference position of the observed point in the image plane (7):

$$\Delta \mathbf{u}(t_n) = \frac{1}{w_n} \mathbf{P} \mathbf{U}(t_n) - \frac{1}{w_{\text{REF}}} \mathbf{P} \mathbf{U}^{\text{REF}} \quad (13)$$

Note that the subtraction (13) is performed in Euclidean coordinates, after the results of the projective transformations (7) have been normalized by the perspective scale factors. Applying the discrete Fourier transform to both sides of Eq. (13) for N images, the amplitude of the image-displacement at ω_k is obtained:

$$\Delta \hat{\mathbf{u}}(\omega_k) = \frac{1}{N} \sum_{n=0}^{N-1} \left(\frac{1}{w_n} \mathbf{P} \mathbf{U}(t_n) - \frac{1}{w_{\text{REF}}} \mathbf{P} \mathbf{U}^{\text{REF}} \right) e^{-j2\pi nk/N} \quad (14)$$

where the perspective scale factors w_n and w^{REF} are (8):

$$w_n = \mathbf{p}_3 \mathbf{U}(t_n) \quad (15)$$

$$w^{\text{REF}} = \mathbf{p}_3 \mathbf{U}^{\text{REF}} \quad (16)$$

The dimensions of the observed object might not be negligible compared to the distance between the object and the camera, which means the effect of perspective on the location of imaged points should generally be considered [23]. As the spatial position of the observed point is $\mathbf{U}(t_n) = \Delta\mathbf{U}(t_n) + \mathbf{U}^{\text{REF}}$ and the relative displacements $\Delta\mathbf{U}$ in high-frequency vibrations are typically some orders of magnitude smaller in comparison, it is therefore reasonable to assume:

$$\mathbf{p}_3 (\Delta\mathbf{U} + \mathbf{U}^{\text{REF}}) \approx \mathbf{p}_3 \mathbf{U}^{\text{REF}} \quad (17)$$

Consequently, from Eq. (15) and (16), it follows:

$$w_n \approx w^{\text{REF}} \quad \text{for } n \in [0, N-1] \quad (18)$$

This simplifies the Eq. (14):

$$\begin{aligned} \Delta\hat{\mathbf{u}}(\omega_k) &= \frac{1}{w^{\text{REF}}} \mathbf{P} \frac{1}{N} \sum_{n=0}^{N-1} (\mathbf{U}(t_n) - \mathbf{U}^{\text{REF}}) e^{-j2\pi nk/N} \\ &= \frac{1}{w^{\text{REF}}} \mathbf{P} \frac{1}{N} \sum_{n=0}^{N-1} \Delta\mathbf{U}(t_n) e^{-j2\pi nk/N} \\ &= \frac{1}{w^{\text{REF}}} \mathbf{P} \Delta\mathbf{U}(\omega_k) \end{aligned} \quad (19)$$

Comparing the result of Eq. (19) with the general equation of perspective camera projection (7), we see that by transforming image-based displacement measurements $\Delta\mathbf{u}(t_n)$, into the frequency domain, we obtain a perspective transform of the (relative) spatial displacement amplitude $\Delta\mathbf{U}(\omega_k)$, which carries our desired information. It should be noted, however, that the scale factor w^{REF} was factored out of the summation (19), and the difference $\mathbf{U}(t_n) - \mathbf{U}^{\text{REF}}$ was obtained in homogeneous coordinates (6). While it still carries the same information of spatial motion, the last homogeneous coordinate of $\Delta\mathbf{U}(t_n)$ was also subtracted, and the result of Eq. (19), after normalization with the perspective scale factor w^{REF} (see Section 2.2), is not a correct Euclidean representation of $\Delta\mathbf{U}(\omega_k)$.

To get a frequency-domain image of the deflected point with the correct perspective scaling, the relative displacement amplitudes $\Delta\hat{\mathbf{u}}(\omega_k)$ (19) must be translated back to their reference image locations \mathbf{u}^{REF} , while the spatial points $\Delta\mathbf{U}(\omega_k)$ and \mathbf{U}^{REF} are still in homogeneous coordinates:

$$\begin{aligned} \hat{\mathbf{u}}(\omega_k) &= \Delta\hat{\mathbf{u}}(\omega_k) + \mathbf{u}^{\text{REF}} \\ &= \frac{1}{w^{\text{REF}}} \mathbf{P} (\Delta\mathbf{U}(\omega_k) + \mathbf{U}^{\text{REF}}) \end{aligned} \quad (20)$$

where the Euclidean representation of:

$$\Delta \mathbf{U}(\omega_k) + \mathbf{U}^{\text{REF}} = \mathbf{U}(\omega_k) \quad (21)$$

can be interpreted as the 3D position of the observed point after displacement in the frequency domain. Assuming the displacement amplitude $\Delta \mathbf{U}(\omega_k)$ is small (17), the actual perspective scale factor (8) when projecting $\mathbf{U}(\omega_k)$ into the image plane can be approximated by w^{REF} , which equals the perspective scale factor in the Eq. (20). The equation of perspective-camera projection of harmonic motion in the frequency domain for small displacements therefore is:

$$\hat{\mathbf{u}}(\omega_k) = \frac{1}{w^{\text{REF}}} \mathbf{P} \mathbf{U}(\omega_k) \quad (22)$$

The significance of the derived Eq. (22) is that it, for a single camera view, assuming small displacements, relates the frequency-domain image of the deflected geometry $\hat{\mathbf{u}}(\omega_k)$, to the unknown spatial position of the displaced point at frequency ω_k , $\mathbf{U}(\omega_k)$ (21), by the perspective-camera transformation (7). Observing the same point in multiple camera views, the three unknown coordinates of $\mathbf{U}(\omega_k)$ can therefore be recovered by multiview triangulation.

3.1. Multiview triangulation in the frequency domain

For each view \mathbf{P}_j in the multiview measurement, frequency-domain images $\hat{\mathbf{u}}_j(\omega_k) = \{\hat{u}_{jk}, \hat{v}_{jk}, 1\}^T$ of the observed point are constructed using image-based displacement measurements (see Section 2.1). Based on Eq. (22), two equations (10) can be written for each distinct camera view:

$$\begin{aligned} (\hat{u}_{jk} \mathbf{p}_j^3 - \mathbf{p}_j^1) \mathbf{U}(\omega_k) &= 0 \\ (\hat{v}_{jk} \mathbf{p}_j^3 - \mathbf{p}_j^2) \mathbf{U}(\omega_k) &= 0 \end{aligned} \quad (23)$$

In a n -view setup, the homogeneous system of equations (23) is solved by the least-squares method, e.g. by singular value decomposition of the $(2n \times 4)$ (for four homogeneous coordinates of $\mathbf{U}(\omega_k)$) coefficient matrix \mathbf{A} :

$$\mathbf{A} = \begin{bmatrix} \hat{u}_{1k} \mathbf{p}_1^3 - \mathbf{p}_1^1 \\ \hat{v}_{1k} \mathbf{p}_1^3 - \mathbf{p}_1^2 \\ \vdots \\ \hat{u}_{nk} \mathbf{p}_n^3 - \mathbf{p}_n^1 \\ \hat{v}_{nk} \mathbf{p}_n^3 - \mathbf{p}_n^2 \end{bmatrix} \quad (24)$$

and the 3D coordinates $\mathbf{U}(\omega_k)$ are obtained by normalizing the singular vector corresponding to the smallest singular value of \mathbf{A} , so that the fourth homogeneous coordinate of $\mathbf{U}(\omega_k)$ is equal to 1 [23].

After performing multiview triangulation over the entire frequency range, the amplitude spectrum of the observed point's harmonic motion can finally be obtained from (21):

$$\Delta \mathbf{U}(\omega_k) = \mathbf{U}(\omega_k) - \mathbf{U}^{\text{REF}} \quad \text{for } k \in [0, N - 1] \quad (25)$$

The reference location of the observed point \mathbf{U}^{REF} therefore must be known; e.g. it can be obtained by multiview triangulation of the initial image positions of the analysed points $\mathbf{u}_j^{\text{REF}}$.

4. Multiview deflection-shape identification with triangulation in the frequency domain

Here a method is proposed where the 3D operation deflection shapes $\mathbf{X}(\omega)$ of a linear, time-invariant mechanical system are identified in a multiview measurement, utilizing a single, moving high-speed camera. Multiple image sequences of the system's response under stationary excitation are acquired from various views and at different points in time at a constant frame-rate. This can be achieved either by moving the measured object or repositioning the high-speed camera to obtain the desired multiview configuration.

After the imaging system has been calibrated using the initial images of the acquired sequence in each particular point of view (see Section 2.2), an arbitrary set of M points \mathbf{U}_i on the surface of the observed object is selected for ODS analysis. The amplitude spectra of the selected points' harmonic motion in Eq. (25) constitute the ODS to be calculated:

$$\mathbf{X}(\omega_k) = \Delta \mathbf{U}_i(\omega_k) \quad \text{for } i \in [0, M - 1] \quad (26)$$

By projecting each of the selected points $\mathbf{U}_i^{\text{REF}}$ from the 3D model into every acquired camera view j and rounding the results to the nearest integer pixel locations, the reference image points for image-based displacement identification are determined:

$$\mathbf{u}_{ij}^{\text{REF}} = \left[\frac{1}{w_{ij}^{\text{REF}}} \mathbf{P}_j \mathbf{U}_i^{\text{REF}} \right] \quad (27)$$

The acquired image sequences are analysed by either the gradient-based optical flow method (3) or digital image correlation (4) to identify the image-plane displacements $\Delta \mathbf{u}_{ij}(t)$ for every point of interest i in each distinct camera view j (see Fig. 3). The displacement time series $\Delta \mathbf{u}_{ij}(t)$, identified for each point, are transformed into the frequency domain using DFT to obtain $\Delta \hat{\mathbf{u}}_{ij}(\omega_k)$ at particular frequencies of interest.

Since the different camera-view image sequences are not acquired synchronously, the identified image-based displacements are first phase-shifted in the frequency-domain, based on a reference excitation measurement of relative phase between views (e.g. using an accelerometer). In each camera view j , the identified image-plane displacement amplitudes $\Delta \hat{\mathbf{u}}_{ij}(\omega_k)$ are then translated by \mathbf{u}^{REF} (20) to construct the images of the deflected geometry $\hat{\mathbf{u}}_{ij}(\omega_k)$ for triangulation, as illustrated in Fig. 3.

For each point of interest on the structure's surface, a system of equations (24) is now written with all the views of the deflected geometry at frequency ω_k in which the current point is visible. The 3D positions of each displaced point $\mathbf{U}_i(\omega_k)$ is identified by solving an overdetermined system of equations

(24). Finally, the operating-deflection-shape $\mathbf{X}(\omega_k)$ for the observed point i is obtained by (21) (see Fig. 3):

$$\mathbf{X}(\omega_k) = \mathbf{U}_i(\omega_k) - \mathbf{U}_i^{\text{REF}}. \quad (28)$$

The proposed method produces full-field spatial measurements, provided that each selected point of interest on the measured object is observed in at least two distinct camera views. In contrast to the well-established 3D DIC method, where triangulation is performed on time-synchronized image-based displacement measurements, a single, moving high-speed camera is used, and the 3D ODS are here reconstructed by triangulation in the frequency domain.

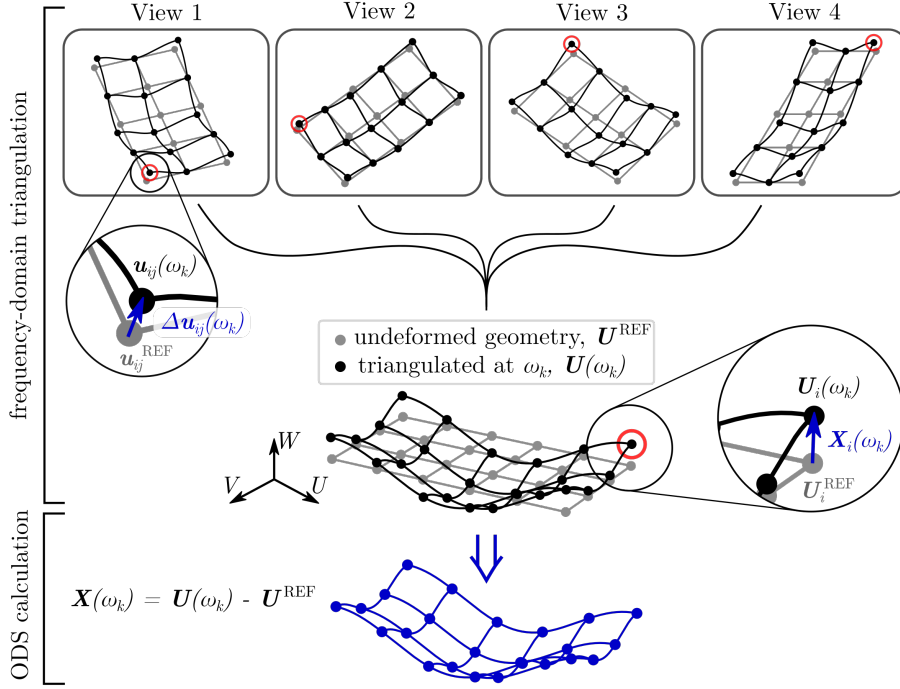


Figure 3: Spatial ODS identification with triangulation in the frequency domain.

The proposed spatial ODS measurement method can be summarized as follows:

1. Image acquisition with a moving camera.
2. Multiview imaging system calibration (Section 2.2) and point-of-interest selection (27).
3. Time-domain image-based displacement identification (Section 2.1).
4. Frequency-domain deflected geometry image construction (20).
5. Frequency-domain multiview triangulation (24).
6. Spatial ODS calculation (28).

5. Experiment

An experiment was devised to demonstrate the use of the proposed method. The operating-deflection-shapes of a 3D specimen were identified using the procedure outlined above.

A 3-plane cubic shell specimen (shown in Fig. 4) was made by bending a 1-mm-thick sheet-metal plate into a concave shape with three symmetrical $200 \text{ mm} \times 200 \text{ mm}$ sides, forming 90-degree angles with one another, and welded along one seam. The corner at the juncture of the three planes was beveled, creating a triangular face of approximately 20 mm in altitude, at equal angles with each of the main sides. A mounting hole 10 mm in diameter was drilled into the centre of this triangular face. A high-contrast speckle pattern was applied to the three sides of the concave object (Fig. 4).

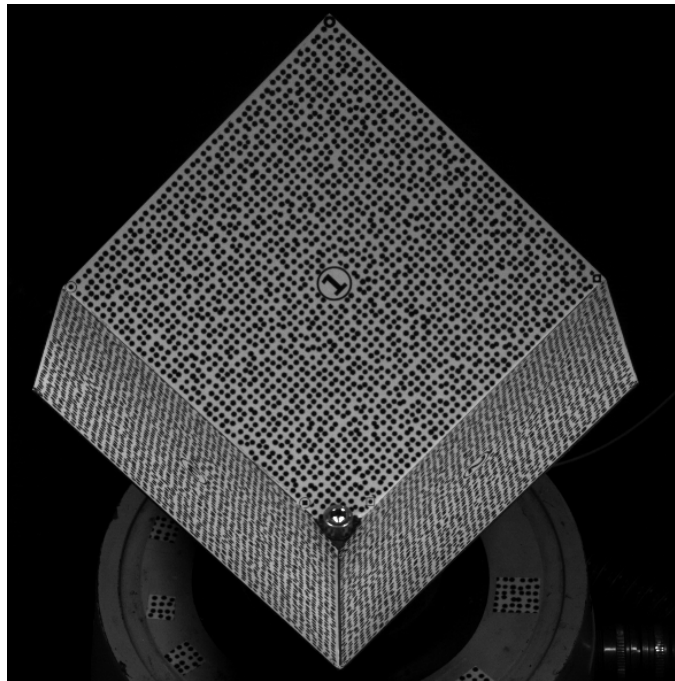


Figure 4: An image of the 3-plane cubic shell, captured in the measurement process.

The 3-plane cubic shell was mounted to a LDS V555 electrodynamic shaker using an M10 bolt and excited with a pseudo-random profile in a frequency band from 25 to 2630 Hz at 3 g RMS, in a direction perpendicular to the beveled corner face. A reference accelerometer (see Fig. 5) was placed on the mounting plate, near the base of the 3-plane cubic shell, to provide a feedback loop for the shaker's controller. Its data was used later in the analysis to measure the relative phase between the excitation in different camera views.

The scene was illuminated using two 50-kilo-lumen LED reflectors. A stationary Photron FASTCAM SA-Z high-speed camera was positioned at approximately 30 angular degrees off the shaker’s vertical axis and 3 m away from the mounting point (Fig. 5). Six image sequences were acquired, rotating the shaker and the observed object 60 degrees around the vertical axis in between each session, resulting in six different views of the process. Each time 20,000 12-bit monochrome frames, 640×640 pixels in size (Fig. 4), were recorded at 20,000 frames per second and saved as 16-bit images, resulting in six one-second multiview measurements for a total of 91.5 of GB image data. Three of the six acquired views are schematically shown in Fig. 5. Twenty images of a checkerboard calibration target of known geometry (Fig. 6) were also recorded while the camera and shaker remained still, to facilitate the identification of the camera’s intrinsic parameters \mathbf{K} .

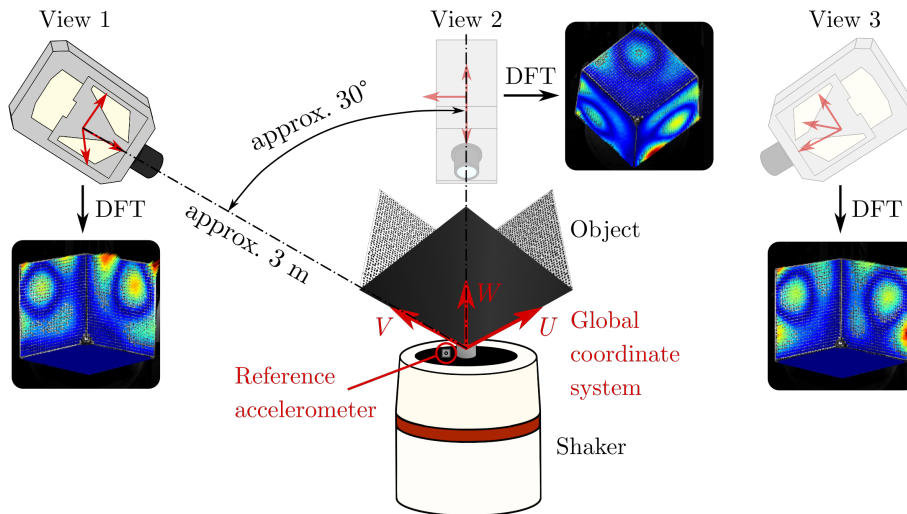


Figure 5: Multiview measurement setup.



Figure 6: Five images of the checkerboard pattern, used in intrinsic parameter estimation.

After the image-acquisition step, the image coordinates of 10 – 15 (depending on the visibility) markers with known 3D positions were identified in the first, reference image of each distinct view. The resulting 2D-3D point corre-

spondences were used as the input to the calibration process. The multiview system’s extrinsic parameters $[\mathbf{R}|\mathbf{t}]_j$ were determined for each view j using an iterative Perspective-n-Point solver, implemented in the OpenCV library [46]. The identified camera positions and orientations are shown in Fig. 7.

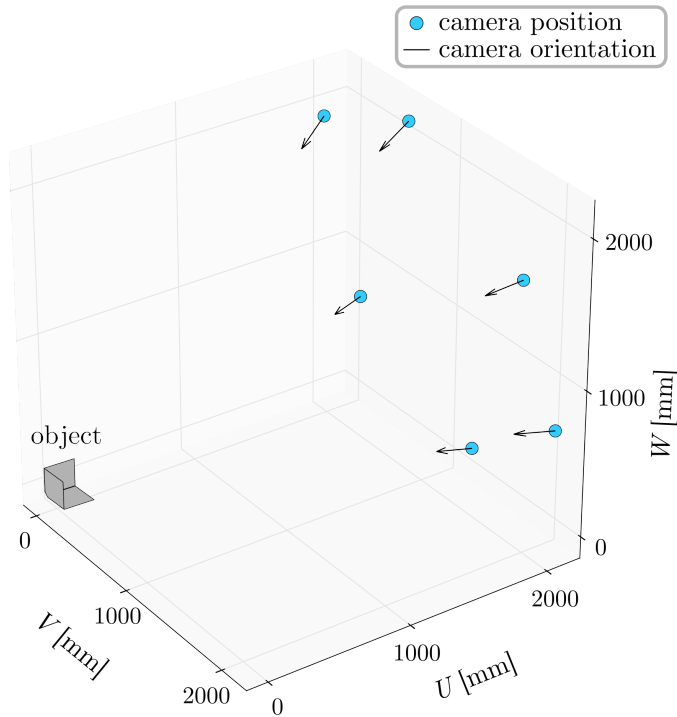


Figure 7: Camera positions and orientations, identified in the calibration process.

Onto each of the three visible faces of the 3-plane cubic shell a regular grid of 30×30 points, offset 6 mm from either edge, was projected (27). This resulted in a total of 2682 points of interest in each image sequence, excluding the 6 points per face that were projected onto the mounting area with no high-contrast pattern applied, and were thus unsuitable for a gradient-based analysis [15].

Image-based displacement identification was performed for the selected grid points. A 3-parameter rigid-body digital image correlation using the Inverse compositional Gauss-Newton image-alignment algorithm [37] and a bicubic interpolation scheme was used. For each selected point, a region of interest of 11×11 pixels was analysed. Although a larger subset size will lead to lower random errors when using DIC, the selected setting was sufficient to showcase the results of the proposed method in our case, while maintaining manageable analysis times. The displacement data for each of the 6 distinct views was transformed into the frequency domain and the resulting image-based displacement measurements used as the input to the linear multiview triangulation algorithm,

as described in Section 4. Operating-deflection-shapes of the 3-plane cubic shell at frequencies up to 1500 Hz were identified. Four examples of the acquired ODS at selected response magnitude peaks are shown in Fig. 8.

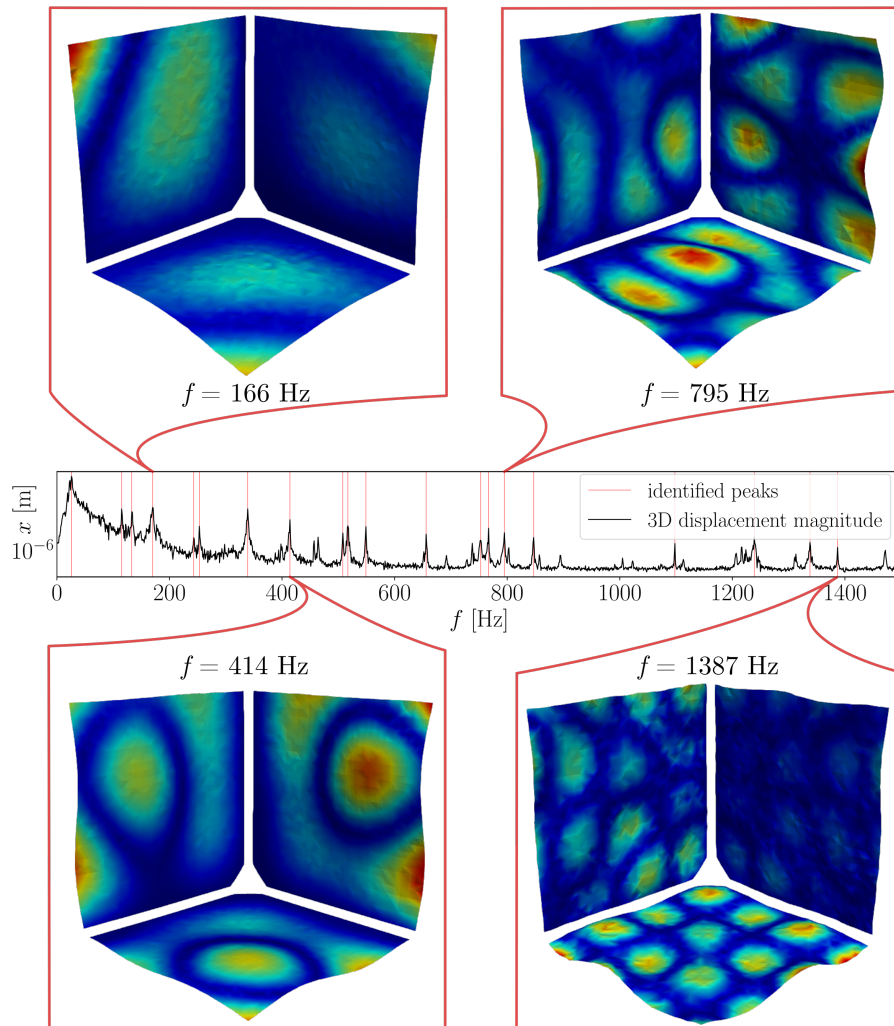


Figure 8: Example ODS at four selected frequencies.

6. Conclusion

A single-camera multiview method for measuring small harmonic motion of arbitrary-shaped specimen is proposed. Its use is demonstrated in an experiment to measure the operating-deflection-shapes in stationary mechanical

vibrations. The introduced method uses only a single moving monochrome high-speed camera and is able to combine several views of the observed motion in a single multiview triangulation step to produce full-field spatial ODS. This is achieved by leveraging the properties of linear, time-invariant mechanical systems subject to random broadband excitation. In contrast to the existing single-camera multiview vibration measurement methods, multiview triangulation is here performed in the frequency domain, eliminating the need for precise time synchronization between the different views.

The central assumptions of the proposed method - linearity of the observed structure and stationarity of the excitation, are also its main limitations. Due to the non-linearity of the perspective camera transform, the normalization of potential discrepancies in excitation amplitudes in different viewpoints before performing frequency-domain triangulation would not be straight-forward. It would also add another step to the already considerably complex post-processing procedure.

Nevertheless, especially in cases where stationary vibration of the specimen is not observable from a single viewpoint, the proposed approach presents a strong alternative to the well-established 3D DIC method, as it offers the possibility of extending the measurement field of view by moving the camera to arbitrary viewpoints around the measured object. This enables vibration measurements of complex-shaped 3D objects without reducing the spatial resolution of the measurement, alleviating one of the main shortcomings of the established stereo DIC method.

Acknowledgement

The authors acknowledge the partial financial support from the Slovenian Research Agency (research core funding no. P2-0263 and project J2-1730).

References

- [1] P. L. Reu, D. P. Rohe, L. D. Jacobs, Comparison of DIC and LDV for practical vibration and modal measurements, *Mechanical Systems and Signal Processing* 86 (2017) 2 – 16, full-field, non-contact vibration measurement methods: comparisons and applications. doi:<https://doi.org/10.1016/j.ymsp.2016.02.006>.
URL <http://www.sciencedirect.com/science/article/pii/S0888327016000339>
- [2] L. O. Heflinger, R. F. Wuerker, R. E. Brooks, Holographic interferometry, *Journal of Applied Physics* 37 (2) (1966) 642–649. doi:[10.1063/1.1708231](https://doi.org/10.1063/1.1708231).
URL <https://doi.org/10.1063/1.1708231>
- [3] O. Lekberg, Electronic speckle pattern interferometry, *Physics in Technology* 11 (1) (1980) 16.
URL <http://stacks.iop.org/0305-4624/11/i=1/a=303>
- [4] R. Ritter, K. Galanulis, D. Winter, E. Müller, B. Breuckmann, Notes on the application of electronic speckle pattern interferometry, *Optics and Lasers in Engineering* 26 (4) (1997) 283 – 299, speckle and Speckle Shearing Interferometry-II. doi:[https://doi.org/10.1016/0143-8166\(95\)00134-4](https://doi.org/10.1016/0143-8166(95)00134-4).
URL <http://www.sciencedirect.com/science/article/pii/S0143816695001344>
- [5] M. N. Helfrick, C. Niezrecki, P. Avitabile, T. Schmidt, 3D digital image correlation methods for full-field vibration measurement, *Mechanical Systems and Signal Processing* 25 (3) (2011) 917 – 927. doi:<https://doi.org/10.1016/j.ymsp.2010.08.013>.
URL <http://www.sciencedirect.com/science/article/pii/S0888327010002980>
- [6] W. Wang, J. E. Mottershead, T. Siebert, A. Pipino, Frequency response functions of shape features from full-field vibration measurements using digital image correlation, *Mechanical Systems and Signal Processing* 28 (2012) 333 – 347, interdisciplinary and Integration Aspects in Structural Health Monitoring. doi:<https://doi.org/10.1016/j.ymsp.2011.11.023>.
URL <http://www.sciencedirect.com/science/article/pii/S0888327011005152>
- [7] T. Ryall, C. Fraser, Determination of structural modes of vibration using digital photogrammetry, *Journal of Aircraft* 39 (1) (2002) 114(6).
- [8] C. Warren, C. Niezrecki, P. Avitabile, Frf measurements and mode shapes determined using image-based 3D point-tracking, in: T. Proulx (Ed.), *Modal Analysis Topics, Volume 3*, Springer New York, New York, NY, 2011, pp. 243–252.

- [9] B. D. Lucas, T. Kanade, An iterative image registration technique with an application to stereo vision, in: Proceedings of the 7th International Joint Conference on Artificial Intelligence - Volume 2, IJCAI'81, Morgan Kaufmann Publishers Inc., San Francisco, CA, USA, 1981, pp. 674–679.
URL <http://dl.acm.org/citation.cfm?id=1623264.1623280>
- [10] T. C. Chu, W. F. Ranson, M. A. Sutton, Applications of digital-image-correlation techniques to experimental mechanics, *Experimental Mechanics* 25 (3) (1985) 232–244. doi:[10.1007/BF02325092](https://doi.org/10.1007/BF02325092).
URL <https://doi.org/10.1007/BF02325092>
- [11] A. Sarrafi, Z. Mao, C. Niezrecki, P. Poozesh, Vibration-based damage detection in wind turbine blades using phase-based motion estimation and motion magnification, *Journal of Sound and Vibration* 421 (2018) 300 – 318. doi:<https://doi.org/10.1016/j.jsv.2018.01.050>.
URL <http://www.sciencedirect.com/science/article/pii/S0022460X18300725>
- [12] Z. M. Aral Sarrafi, Structural operating deflection shape estimation via a hybrid computer-vision algorithm, *Proc.SPIE* 10600 (2018) 10600 – 10600 – 8. doi:[10.1117/12.2296784](https://doi.org/10.1117/12.2296784).
URL <https://doi.org/10.1117/12.2296784>
- [13] J. Javh, J. Slavič, M. Boltežar, Measuring full-field displacement spectral components using photographs taken with a DSLR camera via an analogue fourier integral, *Mechanical Systems and Signal Processing* 100 (2018) 17 – 27. doi:<https://doi.org/10.1016/j.ymsp.2017.07.024>.
URL <http://www.sciencedirect.com/science/article/pii/S0888327017303898>
- [14] B. Pan, Digital image correlation for surface deformation measurement: historical developments, recent advances and future goals, *Measurement Science and Technology* 29 (8) (2018) 082001.
URL <http://stacks.iop.org/0957-0233/29/i=8/a=082001>
- [15] J. Javh, J. Slavič, M. Boltežar, The subpixel resolution of optical-flow-based modal analysis, *Mechanical Systems and Signal Processing* 88 (2017) 89 – 99. doi:<https://doi.org/10.1016/j.ymsp.2016.11.009>.
URL <http://www.sciencedirect.com/science/article/pii/S0888327016304770>
- [16] J. Javh, J. Slavič, M. Boltežar, High frequency modal identification on noisy high-speed camera data, *Mechanical Systems and Signal Processing* 98 (2018) 344 – 351. doi:<https://doi.org/10.1016/j.ymsp.2017.05.008>.
URL <http://www.sciencedirect.com/science/article/pii/S0888327017302637>
- [17] Y.-H. Chang, W. Wang, T. Siebert, J.-Y. Chang, J. E. Mottershead, Basis-updating for data compression of displacement maps from dynamic

- DIC measurements, *Mechanical Systems and Signal Processing* 115 (2019) 405 – 417. doi:<https://doi.org/10.1016/j.ymsp.2018.05.058>.
 URL <http://www.sciencedirect.com/science/article/pii/S0888327018303170>
- [18] S. Dasari, C. Dorn, Y. Yang, A. Larson, D. Mascareñas, A framework for the identification of full-field structural dynamics using sequences of images in the presence of non-ideal operating conditions, *Journal of Intelligent Material Systems and Structures* 29 (17) (2018) 3456–3481. arXiv:<https://doi.org/10.1177/1045389X17754271>, doi:10.1177/1045389X17754271. URL <https://doi.org/10.1177/1045389X17754271>
- [19] Y. Yang, C. Dorn, T. Mancini, Z. Talken, G. Kenyon, C. Farrar, D. Mascareñas, Spatiotemporal video-domain high-fidelity simulation and realistic visualization of full-field dynamic responses of structures by a combination of high-spatial-resolution modal model and video motion manipulations, *Structural Control and Health Monitoring* 25 (8) (2018) e2193, e2193 STC-17-0085.R2. arXiv:<https://onlinelibrary.wiley.com/doi/pdf/10.1002/stc.2193>, doi:10.1002/stc.2193. URL <https://onlinelibrary.wiley.com/doi/abs/10.1002/stc.2193>
- [20] T. J. Beberniss, D. A. Ehrhardt, High-speed 3D digital image correlation vibration measurement: Recent advancements and noted limitations, *Mechanical Systems and Signal Processing* 86 (2017) 35 – 48, full-field, non-contact vibration measurement methods: comparisons and applications. doi:<https://doi.org/10.1016/j.ymsp.2016.04.014>. URL <http://www.sciencedirect.com/science/article/pii/S0888327016300528>
- [21] Z. L. Kahn-Jetter, T. Chu, Three-dimensional displacement measurements using digital image correlation and photogrammic analysis 30 (1990) 10–16.
- [22] K. Patil, J. Baqersad, A. Sheidaei, A multi-view digital image correlation for extracting mode shapes of a tire, in: J. M. Harvie, J. Baqersad (Eds.), *Shock & Vibration, Aircraft/Aerospace, Energy Harvesting, Acoustics & Optics, Volume 9*, Springer International Publishing, Cham, 2017, pp. 211–217.
- [23] R. Hartley, A. Zisserman, *Multiple View Geometry in Computer Vision*, 2nd Edition, Cambridge University Press, New York, NY, USA, 2003.
- [24] J.-J. Orteu, F. Bugarin, J. Harvent, L. Robert, V. Velay, Multiple-camera instrumentation of a single point incremental forming process pilot for shape and 3D displacement measurements: Methodology and results, *Experimental Mechanics* 51 (4) (2011) 625–639. doi:10.1007/s11340-010-9436-1. URL <https://doi.org/10.1007/s11340-010-9436-1>

- [25] Y.-H. C. Chi-Hung Hwang, Wei-Chung Wang, Camera calibration and 3D surface reconstruction for multi-camera semi-circular DIC system, *Proc.SPIE* 8769 (2013) 8769 – 8769 – 8. doi:10.1117/12.2021044.
URL <https://doi.org/10.1117/12.2021044>
- [26] K. Patil, V. Srivastava, J. Baqersad, A multi-view optical technique to obtain mode shapes of structures, *Measurement* 122 (2018) 358 – 367. doi:<https://doi.org/10.1016/j.measurement.2018.02.059>.
URL <http://www.sciencedirect.com/science/article/pii/S0263224118301581>
- [27] V. Srivastava, J. Baqersad, An optical-based technique to obtain operating deflection shapes of structures with complex geometries, *Mechanical Systems and Signal Processing* 128 (2019) 69 – 81. doi:<https://doi.org/10.1016/j.ymsp.2019.03.021>.
URL <http://www.sciencedirect.com/science/article/pii/S0888327019301955>
- [28] B. Pan, L. Yu, Q. Zhang, Review of single-camera stereo-digital image correlation techniques for full-field 3D shape and deformation measurement, *Science China Technological Sciences* 61 (1) (2018) 2–20. doi:10.1007/s11431-017-9090-x.
URL <https://doi.org/10.1007/s11431-017-9090-x>
- [29] M. Pankow, B. Justusson, A. M. Waas, Three-dimensional digital image correlation technique using single high-speed camera for measuring large out-of-plane displacements at high framing rates, *Appl. Opt.* 49 (17) (2010) 3418–3427. doi:10.1364/AO.49.003418.
URL <http://ao.osa.org/abstract.cfm?URI=ao-49-17-3418>
- [30] L. Yu, B. Pan, Single-camera stereo-digital image correlation with a four-mirror adapter: optimized design and validation, *Optics and Lasers in Engineering* 87 (2016) 120 – 128. doi:<https://doi.org/10.1016/j.optlaseng.2016.03.014>.
URL <http://www.sciencedirect.com/science/article/pii/S0143816616300021>
- [31] K. Genovese, L. Casaletto, J. Rayas, V. Flores, A. Martinez, Stereo-digital image correlation (DIC) measurements with a single camera using a biprism, *Optics and Lasers in Engineering* 51 (3) (2013) 278 – 285. doi:<https://doi.org/10.1016/j.optlaseng.2012.10.001>.
URL <http://www.sciencedirect.com/science/article/pii/S0143816612002837>
- [32] S. Xia, A. Gdoutou, G. Ravichandran, Diffraction assisted image correlation: A novel method for measuring three-dimensional deformation using two-dimensional digital image correlation, *Experimental Mechanics* 53 (5) (2013) 755–765. doi:10.1007/s11340-012-9687-0.
URL <https://doi.org/10.1007/s11340-012-9687-0>

- [33] L. Yu, B. Pan, Full-frame, high-speed 3D shape and deformation measurements using stereo-digital image correlation and a single color high-speed camera, *Optics and Lasers in Engineering* 95 (2017) 17 – 25. doi:<https://doi.org/10.1016/j.optlaseng.2017.03.009>.
URL <http://www.sciencedirect.com/science/article/pii/S014381661730060X>
- [34] L. Yu, B. Pan, Single-camera high-speed stereo-digital image correlation for full-field vibration measurement, *Mechanical Systems and Signal Processing* 94 (2017) 374 – 383. doi:<https://doi.org/10.1016/j.ymsp.2017.03.008>.
URL <http://www.sciencedirect.com/science/article/pii/S088832701730122X>
- [35] T. Durand-Texte, E. Simonetto, S. Durand, M. Melon, M.-H. Moulet, Vibration measurement using a pseudo-stereo system, target tracking and vision methods, *Mechanical Systems and Signal Processing* 118 (2019) 30 – 40. doi:<https://doi.org/10.1016/j.ymsp.2018.08.049>.
URL <http://www.sciencedirect.com/science/article/pii/S0888327018305934>
- [36] D. M. F. C. Quentin Davis, Statistics of subpixel registration algorithms based on spatiotemporal gradients or block matching, *Optical Engineering* 37 (1998) 37 – 37 – 9. doi:10.1117/1.601966.
URL <https://doi.org/10.1117/1.601966>
- [37] B. Pan, K. Li, W. Tong, Fast, robust and accurate digital image correlation calculation without redundant computations, *Experimental Mechanics* 53 (7) (2013) 1277–1289. doi:10.1007/s11340-013-9717-6.
URL <https://doi.org/10.1007/s11340-013-9717-6>
- [38] M. A. Sutton, J. J. Orteu, H. Schreier, Image correlation for shape, motion and deformation measurements: basic concepts, theory and applications, Springer Science & Business Media, New York, 2009.
- [39] Z. Zhang, A flexible new technique for camera calibration, *IEEE Transactions on Pattern Analysis and Machine Intelligence* 22 (11) (2000) 1330–1334. doi:10.1109/34.888718.
- [40] K. Genovese, L. Cortese, M. Rossi, D. Amodio, A 360-deg digital image correlation system for materials testing, *Optics and Lasers in Engineering* 82 (2016) 127 – 134. doi:<https://doi.org/10.1016/j.optlaseng.2016.02.015>.
URL <http://www.sciencedirect.com/science/article/pii/S0143816616000531>
- [41] F. Moreno-Noguer, V. Lepetit, P. Fua, Accurate non-iterative $O(n)$ solution to the PnP problem, 2007 Ieee 11Th International Conference On Computer Vision, Vols 1-6 (2007) 2252–2259.
URL <http://infoscience.epfl.ch/record/179767>

- [42] R. I. Hartley, P. Sturm, Triangulation, *Computer Vision and Image Understanding* 68 (2) (1997) 146 – 157. doi:<https://doi.org/10.1006/cviu.1997.0547>.
URL <http://www.sciencedirect.com/science/article/pii/S1077314297905476>
- [43] N. A. J. Lieven, D. J. Ewins, N. M. M. Maia, J. M. M. Silva, Modal analysis identification techniques, *Philosophical Transactions of the Royal Society of London. Series A: Mathematical, Physical and Engineering Sciences* 359 (1778) (2001) 29–40. arXiv:<https://royalsocietypublishing.org/doi/pdf/10.1098/rsta.2000.0712>, doi:10.1098/rsta.2000.0712.
URL <https://royalsocietypublishing.org/doi/abs/10.1098/rsta.2000.0712>
- [44] M. H. Richardson, P. L. McHargue, Operating deflection shapes from time versus frequency domain measurements, in: *Proceedings of the International Modal Analysis Conference, SEM Society for Experimental Mechanics INC, 1993*, pp. 581–581.
- [45] H. Vold, B. Schwarz, M. Richardson, Measuring operating deflection shapes under non-stationary conditions, in: *18th International Modal Analysis Conference, Texas San Antonio, Texas, 2000*.
- [46] OpenCV, Open Source Computer Vision Library, <https://github.com/opencv/opencv> (2018).